THREE DIMENSIONAL NUCLEI SEGMENTATION AND CLASSIFICATION OF FLUORESCENCE MICROSCOPY IMAGES

Shuo Han[*]   *Soonam Lee*[*]   *Alain Chen*[*]   *Changye Yang*[*]
Paul Salama[†]   *Kenneth W Dunn*[‡]   *Edward J. Delp*[*]

[*]Video and Image Processing Laboratory
School of Electrical and Computer Engineering
Purdue University
West Lafayette, Indiana

[†]Department of Electrical and
Computer Engineering
Indiana University-Purdue University
Indianapolis, Indiana

[‡]Division of Nephrology
School of Medicine
Indiana University
Indianapolis, Indiana

ABSTRACT

Segmentation and classification of cell nuclei in fluorescence 3D microscopy image volumes are fundamental steps for image analysis. However, accurate cell nuclei segmentation and detection in microscopy image volumes are hampered by poor image quality, crowding of nuclei, and large variation in nuclei size and shape. In this paper, we present an unsupervised volume to volume translation approach adapted from the Recycle-GAN using modified Hausdorff distance loss for synthetically generating nuclei with better shapes. A 3D CNN with a regularization term is used for nuclei segmentation and classification followed by nuclei boundary refinement. Experimental results demonstrate that the proposed method can successfully segment nuclei and identify individual nuclei.

Index Terms— nuclei segmentation, fluorescence microscopy, convolutional neural network, generative adversarial network

1. INTRODUCTION

With the development of fluorescence microscopy, such as two-photon microscopy and multi-photon microscopy, large 3D volumes of microscopy data with deep penetration depth into tissue are possible [1]. For quantitative analysis of biomedical structures in these 3D volumes, cell nuclei have been extensively used since they form a highly organized structure and can easily be labeled with fluorescent markers [2]. By analyzing volumetric data with nuclei information, important information such as cell location, cell density, and cell type can be obtained.

There have been several methods developed for nuclei segmentation and classification. One example is the use of watershed [3] which is a combination of region growing and edge detection to achieve individual nuclei segmentation and classification. Another popular method for nuclei segmentation is active contours [4] which minimizes an energy functional iteratively to fit a contour to objects of interest. An early version of the edge-based active contours [4] tends to fail to segment objects in fluorescence microscopy because of its sensitiveness to initial contour placement and vulnerability to noise. Region-based active contours was introduced in [5] that seeks an energy balance between foreground and background regions. Region-based active contours was extended to 3D by developing an inhomogeneity intensity correction in [6]. Meanwhile, CellProfiler software [7] was developed for biomedical image analysis including cell segmentation and classification.

Convolutional neural networks (CNN) has been popular to address various problems in medical imaging [8]. U-Net [9] is one of the most successful 2D CNN architectures used for medical image segmentation. U-Net uses an encoder-decoder architecture that transfers entire feature maps from each encoder layer to the corresponding decoder layer. Nuclei classification, segmentation, and detection using a combination of densely connected recurrent convolutional network and regression model with recurrent residual convolutional neural network based on U-Net was described in [10]. A 3D nuclei segmentation method that utilizes the SegNet [11] with data augmentation followed by a 3D watershed was presented in [12]. Additionally, a 3D U-Net which extends U-Net [9] to 3D to achieve volumetric image segmentation was introduced in [13]. Similarly, a V-Net which uses the Dice coefficient as a loss term in training to achieve volumetric segmentation was demonstrated in [14]. More recently, the Hausdorff distance which is typically used for the shape similarity measure for evaluating segmentation performance [15] was introduced as a loss term for locating objects [16] as well as medical image segmentation [17].

The previously discussed methods require huge volumes of manually annotated groundtruth for training. To address this problem, an approach to generate synthetic groundtruth and corresponding synthetic data was needed. The use of the cycle-consistent adversarial networks (CycleGAN) [18] for generating realistic 3D images from unpaired training data has shown promising results in [19] and [20]. Hence, we introduced a two-stage method known as spatially constrained cycle-consistent adversarial networks (SpCycleGAN) [21] that incorporates a spatially constrained loss to the CycleGAN to prevent misalignment between synthetically generated groundtruth volume and corresponding synthetically generated microscopy volume followed by 3D segmentation. This SpCycle-GAN was utilized for nuclei detection and counting in [22] and further extended in [23] to utilize three directions in a volume along with axial, coronal, and sagittal sections (3-Way SpCycleGAN) to incorporate 3D information. One drawback of the SpCycleGAN and the 3-Way SpCycleGAN is that they are not fully 3D but 2D based methods. They generate synthetic groundtruth volumes and corresponding microscopy volumes that are not perfectly aligned in 3D. To address this problem, the Recycle-GAN [24] was introduced which adds a third dimension to the CycleGAN [18] to achieve video-to-video style transfer.

In this paper, we describe a 3D segmentation and classification method to segment and identify individual nuclei in fluorescence microscopy volumes without having groundtruth volumes. Three dimensional synthetic data is generated using the Recycle-GAN [24] with the Hausdorff distance loss introduced in [17] to preserve the shape of individual nuclei. A 3D CNN network is then trained us-
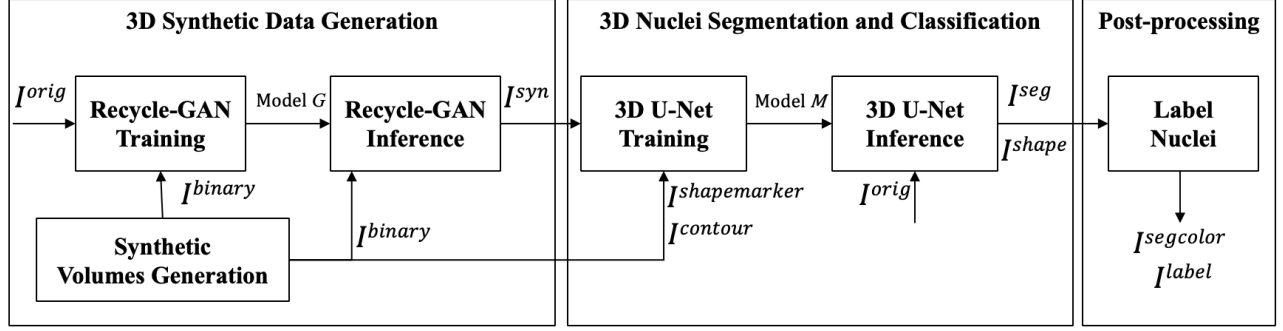
Fig. 1. Block diagram of the proposed nuclei segmentation and classification method

ing the 3D synthetic data to segment and classify different kinds of nuclei structures. Our method is evaluated using hand segmented groundtruth volumes of real fluorescence microscopy data from a rat kidney. Our data was collected using two-photon microscopy with nuclei labeled with Hoechst 33342 staining.

2. PROPOSED METHOD

Figure 1 shows the block diagram of our proposed method for nuclei segmentation and classification. In this paper, a 3D image volume of size $X \times Y \times Z$ is denoted with I. We use I_{z_p} to represent an xy slice of I at the pth focal plane along the z-direction in a volume. Here, the range of p is $p \in \{1, \ldots, Z\}$. I_{y_q} is a xz slice of I at the qth focal plane along the y-direction with $q \in \{1, \ldots, Y\}$. Similarly, I_{x_r} is a yz slice of I at the rth focal plane along the x-direction with $r \in \{1, \ldots, X\}$. To indicate how a volume is sectioned from I, $I_{\left(r_i:r_f, q_i:q_f, p_i:p_f\right)}$ is used, where the coordinates of x is between $\{r_i, ..., r_f\}$, the coordinates of y is between $\{q_i, ..., q_f\}$, and the coordinate of z is between $\{p_i, ..., p_f\}$. For example, if a subvolume is a xy section from the 100th slice to the 150th slice along the z-direction, the subvolume can be denoted as $I_{\left(1:r_f, 1:q_f, 100:150\right)}$.

Our proposed method is composed of three main steps: 3D synthetic data generation, 3D nuclei segmentation and classification, and post-processing. I^{orig} denotes the original microscopy volume used for training during 3D synthetic data generation and testing during 3D nuclei segmentation and classification. I^{binary} represents the synthetic binary data generated during 3D synthetic data generation, which is used together with I^{orig} to train a Recycle-GAN model G. With a trained model G, I^{syn} can be generated as a synthetic microscopy volume based on the features of I^{orig}. During the generation of I^{binary}, two more synthetic volumes $I^{contour}$ and $I^{shapemarker}$ that are corresponding to I^{binary} are generated. Here, $I^{contour}$ contains the boundary of each nucleus whereas $I^{shapemarker}$ contains the ellipticity as a shape indicator of the nuclei. I^{syn} is paired with I^{binary} to train a 3D U-Net segmentation model M. Also, the corresponding $I^{shapemarker}$ and $I^{contour}$ are used during the training of the model to refine the shape of the segmentation. During the inference of the 3D U-Net, two different initial results volumes I^{seg} and I^{shape} are generated using model M. Here, I^{seg} contains the binary segmentation mask of the nuclei and I^{shape} contains the shape indicator of the nuclei volume. During the post-processing step, I^{seg} and I^{shape} are used to produce the final results of the color-coded segmentation volume $I^{segcolor}$ and the labeled volumed I^{label} which labels each nucleus by its type.

2.1. 3D Synthetic Data Generation

Three dimensional synthetic data generation consists of three stages: the generation of the synthetic volumes, the training of the Recycle-GAN [24], and the inference of the Recycle-GAN. The synthetic volume I^{binary} is created by adding ellipsoidal nuclei candidates with different shape, size, and orientation to the volume at random locations. The range of the shape and size of the synthetic nuclei are appropriately chosen for the original microscopy volume. For i^{th} nucleus with semi-axes $\mathbf{a}_i = \left(a_{i_x}, a_{i_y}, a_{i_z}\right)$ and centroid at $\mathbf{c}_i = (x_i, y_i, z_i)$, $I^{binary,i}$ can be expressed with Eq. (1) as:

$$I^{binary,i} = \begin{cases} 1, & \text{if } \left(\frac{x-x_i}{a_{i_x}}\right)^2 + \left(\frac{y-y_i}{a_{i_y}}\right)^2 + \left(\frac{z-z_i}{a_{i_z}}\right)^2 < 1 \\ 0, & \text{otherwise} \end{cases} \quad (1)$$

where the value of $\mathbf{a}$ is selected from $r \in \{r_{min}, \ldots, r_{max}\}$. Let $a_{i_{min}}$ and $a_{i_{max}}$ represent the minimum and maximum value among $\left(a_{i_x}, a_{i_y}, a_{i_z}\right)$, respectively. Here, the orientation of nuclei is selected with random rotation as described in [25]. For each I^{binary}, two corresponding synthetic volumes $I^{contour}$ and $I^{shapemarker}$ are generated using Eq. (2) and (3) such that

$$I^{contour,i} = \begin{cases} 1, & \text{if } 0.7 < \left(\frac{x-x_i}{a_{i_x}}\right)^2 + \left(\frac{y-y_i}{a_{i_y}}\right)^2 + \left(\frac{z-z_i}{a_{i_z}}\right)^2 < 1 \\ 0, & \text{otherwise} \end{cases}$$
$$(2)$$

$$I^{shapemarker,i} = 255 \cdot \left(\frac{a_{i_{max}} - a_{i_{min}}}{r_{max} - r_{min}}\right) \cdot I^{binary,i} \quad (3)$$

The generated I^{binary} is then processed with a 3D Gaussian filter with $\sigma = 2$ to simulate microscopy's image acquisition process where the target object is convolved with a 3D point spread function (PSF) [23]. The blurred I^{binary} volume is then used together with I^{orig} to train the Recycle-GAN.

The Recycle-GAN [24] is an extension of the CycleGAN [18] by replacing the cycle consistency loss with a recurrent loss and a recycle loss. The main difference between the CycleGAN and the Recycle-GAN is that the Recycle-GAN was originally proposed for use in the generation of synthetic videos using ordered sequential frames of images. Here, we used a 3D image volume instead of a video, which means the ordered sequential images are a series of images taken along the z direction. In addition to the generative models G_1 and G_2 and the discriminative models D_1 and D_2, the Recycle-GAN uses the predictive models P_1 and P_2 to predict the current frame based on S previous frames. For our method, we modified the predictive model to take an ordered series of S images (I_z) along the z direction in the spatial domain instead of the temporal domain. The recurrent loss is used to measure the prediction accuracy of the predictive model. Similarly, the recycle loss is a modified version of the cycle consistency loss which incorporates the predictive model for image reconstruction.

Eq. (4) shows the training losses of our proposed method. Note that $\lambda_1, ..., \lambda_5$ are the controllable coefficients for each loss term. G_1 is a generative model that can transfer I^{binary} to I^{syn} whereas G_2 is a generative model that can transfer I^{syn} to I^{binary}. P_1 is a generative model that can predict $I_{z_{p+S+1}}^{binary}$ from $I_{z_p:z_{p+S}}^{binary}$ whereas P_2 is a generative model that can predict $I_{z_{p+S+1}}^{syn}$ from $I_{z_p:z_{p+S}}^{syn}$. Additionally, D_1 is a discriminative model that distinguishes between I^{binary} and $P_1(G_2(I^{syn}))$. Also, D_2 is a discriminative model that distinguishes between I^{syn} and $P_2(G_1(I^{binary}))$.

$$\mathcal{L}(G_1, G_2, D_1, D_2, P_1, P_2, S)\{I^{binary}, I^{syn}\}$$
$$=\mathcal{L}_{\text{GAN}}(G_1, D_2) + \mathcal{L}_{\text{GAN}}(G_2, D_1)$$
$$+\lambda_1 \cdot \mathcal{L}_{recycle}(G_1, G_2, P_2, S) + \lambda_2 \cdot \mathcal{L}_{recycle}(G_2, G_1, P_1, S)$$
$$+\lambda_3 \cdot \mathcal{L}_{recurrent}(P_1, S) + \lambda_4 \cdot \mathcal{L}_{recurrent}(P_2, S)$$
$$+\lambda_5 \cdot \mathcal{L}_{contour}(G_2, P_1, S) \tag{4}$$

Moreover, we utilize a contour constraint loss term $\mathcal{L}_{contour}$ based on estimating the Hausdorff distance from the distance transform as described in [17]. Since the Hausdorff distance estimates the difference between two boundaries, adding this loss could refine the shape of the synthetic generated nuclei. We define the distance transform as a function $F_{DT}: I^{binary} \to F_{DT}(I^{binary})$ which finds the Euclidean distance between each voxel and its nearest background voxel. $\mathcal{L}_{contour}$ works by penalizing large errors at the boundaries of nuclei so that the generated nuclei have refined shape by minimizing $\mathcal{L}_{contour}$ as in Eq. (5):

$$\mathcal{L}_{contour}(G_2, P_1, S)\{I^{binary}, I^{syn}\} =$$
$$\mathbb{E}_{I^{binary}}\{(\|I^{binary} - P_1(G_2(I^{syn}))\|_2 \cdot F_{DT}(I^{binary})^2$$
$$+\|I^{binary} - P_1(G_2(I^{syn}))\|_2 \cdot F_{DT}(P_1(G_2(I^{syn})))^2)^{1/2}\} \tag{5}$$

During the Recycle-GAN inference, the synthetic microscopy volume, I^{syn}, is generated from using the model G on the synthetic binary volume, I^{binary}. For each synthetic volume I^{binary}, the corresponding synthetic volumes $I^{contour}$ and $I^{labelmarker}$ are generated. I^{binary} and I^{syn} form a paired set of volumes for the training of the 3D U-Net segmentation model.

2.2. 3D Nuclei Segmentation and Classification

Three dimensional nuclei segmentation and classification consists of 3D U-Net training, 3D U-Net inference, and post-processing. As shown in Figure 1, we utilize a paired set I^{syn} and I^{binary} to train a 3D U-Net and obtain a generative model M_1. Here, the model M_1 is a function mapping nuclei in I^{orig} to the segmented volume in I^{seg}. Another paired set I^{syn} and $I^{shapemarker}$ are used to train a 3D U-Net model M_2. The model M_2 is a function that maps nuclei in I^{orig} to its corresponding shape information in I^{shape}. $I^{contour}$ is utilized during the training of the model M_1 and M_2 for refining the shape of nuclei in the segmented volume. I^{seg} and I^{shape} are then used to generate nuclei segmentation volume $I^{segcolor}$ and I^{label}.
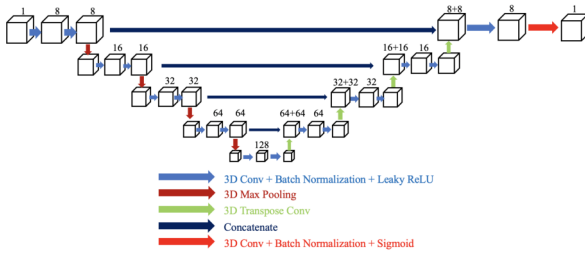

Fig. 2. Architecture of the modified 3D U-Net

The architecture of the modified 3D U-Net [13] for nuclei segmentation and classification is shown in Figure 2. Each convolutional layer contains a 3D convolution with filter size of $3 \times 3 \times 3$,

a batch normalization, and a rectified-linear unit (ReLU) activation function. A 3D max-pooling of stride 2 with a window size of $2 \times 2 \times 2$ is used for the downsampling procedure. Similarly, a 3D transposed convolution is used for an upsampling procedure. Corresponding encoder and decoder layers are connected with a concatenation operation to preserve spatial information. The training loss here is the same as described in [21] but with an addition of $\mathcal{L}_{MSE}\{I^{contour}, C(I^{seg})\}$, where $C(\cdot)$ is a Canny [26] edge function that finds the edges of a binary volume.

3. EXPERIMENTAL RESULTS

To test our proposed method, we used two rat kidney data sets denoted as Data-I and Data-II[1]. The size of Data-I and Data-II are $X \times Y \times Z = 512 \times 512 \times 415$ voxels and $X \times Y \times Z = 512 \times 512 \times 32$ voxels. A volume size of $128 \times 128 \times 128$ was selected for the Recycle-GAN training for both data sets. By inferencing with the trained model G, 10 synthetic microscopy volumes were generated, with the size being $128 \times 128 \times 128$. Those volumes were divided into 80 pairs of smaller volumes ($64 \times 64 \times 64$). These 80 pairs of synthetic volumes are then used for the training of model M_1 and M_2. Also, $\lambda_1 = 1, \lambda_2 = \lambda_3 = \lambda_4 = 10, \lambda_5 = 0.1, S = 10$ in Eq. (4) were experimentally selected and used for both data sets. Note that we used PyTorch to implement our network architecture. We used Adam optimizer [27] with a learning rate of 0.0001.
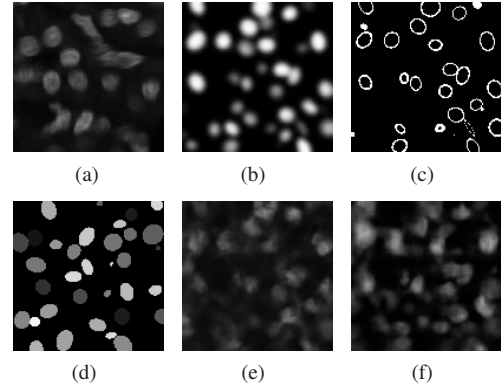

Fig. 3. Comparison of slices of the synthetic volumes with the original volume of Data-I (a) I^{orig} (b) I^{binary} with Gaussian blur, (c) $I^{contour}$, (d) $I^{shapemarker}$ at another plane, (e) I^{syn} from Recycle-GAN, (f) I^{syn} from Recycle-GAN with the Hausdorff distance loss

Figure 3 shows the synthetic binary images, the corresponding synthetic contour images, and the corresponding synthetic microscopy images. An original microscopy image is shown in Figure 3(a). An example slice of the synthetic $I^{shapemarker}$ is displayed in Figure 3(d). It can be observed that the synthetic microscopy images look like the original microscopy image with respect to nuclei characteristics. Then, we use the synthetic images obtained from model G to train a segmentation network and a classification network. In particular, since a 3D U-Net model M_1 is trained with paired sets I^{binary} and I^{syn}, this model is able to do segmentation. Similarly, the model M_2 is trained with paired sets $I^{shapemarker}$ and I^{syn} so that this model is able to generate I^{shape} from I^{orig} which contains the shape information of the nuclei. Lastly, post-processing on I^{seg} is done by using watershed in 3 dimensions and labeling the nuclei with different colors with 3D connected component. Then, a distance transform followed by thresholding is done on I^{seg} to obtain

---

[1]All imaging data used for this paper was obtained from animals and was collected at the Indiana Center for Biological Microscopy at the Indiana University Medical School. The studies used to collect this data were approved by the Indiana University animal use committee.
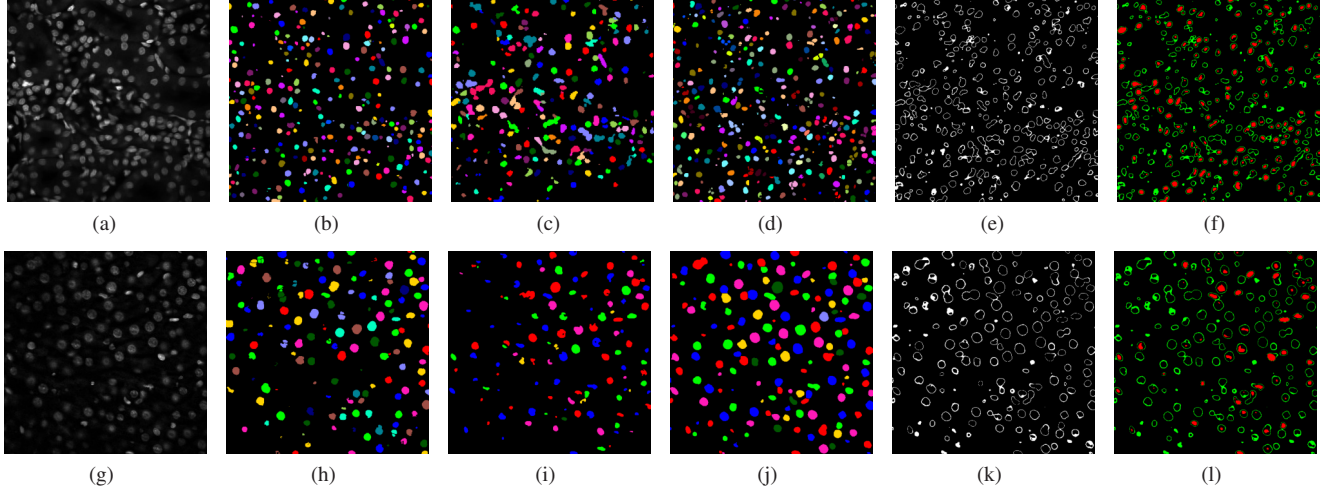
Fig. 4. Comparison of slices of the original image volume and results obtained from SpCycleGAN [21], CellProfiler [7], and our proposed method of Data-I: (a) I^{orig}, (b) segmentation result from SpCycleGAN, (c) segmentation result from CellProfiler, (d) $I^{segcolor}$ from our method, (e) contour image from our method, (f) I^{label} image from our method, Data-II: (g) I^{orig}, (h) segmentation result from SpCycleGAN, (i) segmentation result from CellProfiler, (j) $I^{segcolor}$ from our method, (k) contour image from our method, (l) I^{label} from our method

the contour images. The post-processing on I^{shape} is done by the Gaussian blurring with $\sigma = 2$ followed by thresholding with empirically selected thresholds. The thresholded images are then overlaid with the contour images to obtain I^{label}.

Our proposed method is compared with SpCycleGAN [21] and CellProfiler [7]. Note that both methods are tuned to produce the best results possible. Also, the SpCycleGAN is used together with a modified 3D U-Net whose training loss includes the Binary Cross Entropy (BCE) loss and the Dice loss [21]. Figure 4 shows the comparison of the color-coded images obtained from the SpCycleGAN [21] with 3D U-Net for segmentation, CellProfiler [7] using the watershed for segmentation, and our proposed method. It is observed that the SpCycleGAN method tends to miss multiple nuclei and cannot capture the correct shape of the elongated nuclei while the CellProfiler method cannot distinguish and label a cluster of nuclei. Our method can find nuclei at the correct location with more accurate nuclei shape. Figure 4(e) shows the contour image generated from 3D U-Net and post-processing which labels the boundary of detected nuclei. Figure 4(f) is an example slice of I^{label} which exhibits nuclei classified as non-sphere shaped nuclei. The centroids of those nuclei are highlighted in red and the nuclei boundaries overlaid onto those centroids shown in Figure 4(e) are highlighted in green. It can be observed that nuclei with red labels have more ellipsoidal shapes.

Table 1. Evaluation of the proposed method of Data-I and Data-II

	Microscopy Data-I			Microscopy Data-II		
	P	R	$F1$	P	R	$F1$
[7]	71.32%	65.25%	68.15%	81.21%	73.63%	77.23%
[21]	86.77%	68.62%	76.64%	89.32%	87.45%	88.37%
Proposed	76.99%	88.04%	82.14%	90.16%	95.82%	92.90%

We used the object-based evaluation we presented in [15] to find the accuracy of the nuclei segmentation. Small objects removal is done to remove objects with small sizes (fewer than 50 voxels). Manually annotate groundtruth is obtained using the ITK-SNAP [28] which generated distinct labels for each nucleus. The groundtruth we used here are a subvolume of Data-I with a size of $128 \times 128 \times 64$ and a subvolume of Data-II with a size of $256 \times 256 \times 32$. A true-positive, N_{TP}, is obtained if a nucleus has at least 50% overlap with its matching groundtruth. A false-positive, N_{FP}, is obtained if a

nucleus has less than 50% overlap with its matching groundtruth. A false-negative, N_{FN}, is obtained if a nucleus in the groundtruth can not find a matching nucleus in the segmentation result. The F1 score (F1), Precision (P), and Recall (R) are then obtained as in [15]. Table 1 shows that our proposed method performs better than the compared methods with a higher F1 score. The object-based evaluation demonstrates that our method can segment and locate nuclei correctly.

4. CONCLUSIONS

In this paper, we have demonstrated an approach for segmenting and classifying nuclei in 3D microscopy image volumes using synthetic training data. We first generated synthetic microscopy image volumes using the Recycle-GAN with a loss term using the Hausdorff distance. With the use of Recycle-GAN, three dimensional information can be fully utilized for generating synthetic image volumes. The use of the Hausdorff distance based loss function can refine the boundary of the generated nuclei by penalizing inaccuracies occurring around the boundaries of the synthetic nuclei. We then employed a 3D CNN for nuclei segmentation and another 3D CNN for nuclei classification based on the shape of the nuclei. The 3D CNN trained on synthetic data was capable of segmenting nuclei and generating volumes with nuclei shape information without fine-tuning. Our proposed method has the advantage to preserve nuclei shape and can be used to separate different types of nuclei within the same volume without additional information. In the future, we plan to produce groundtruth volumes with nuclei type information and evaluate the accuracy of nuclei type classification.

5. REFERENCES

[1] C. Vonesch, F. Aguet, J. Vonesch, and M. Unser, "The colored revolution of bioimaging," *IEEE Signal Processing Magazine*, vol. 23, no. 3, pp. 20–31, May 2006.

[2] E. Meijering, "Cell segmentation: 50 years down the road," *IEEE Signal Processing Magazine*, vol. 29, no. 5, pp. 140–145, September 2012.

[3] L. Vincent and P. Soille, "Watersheds in digital spaces: an efficient algorithm based on immersion simulations," *IEEE Transactions on Pattern Analysis and Machine Intelligence*, vol. 13, no. 6, pp. 583–598, June 1991.

[4] M. Kass, A. Witkin, and D. Terzopoulos, "Snakes: Active contour models," *International Journal of Computer Vision*, vol. 1, no. 4, pp. 321–331, January 1988.

[5] T. F. Chan and L. A. Vese, "Active contours without edges," *IEEE Transactions on Image Processing*, vol. 10, no. 2, pp. 266–277, February 2001.

[6] S. Lee, P. Salama, K. W. Dunn, and E. J. Delp, "Segmentation of fluorescence microscopy images using three dimensional active contours with inhomogeneity correction," *Proceedings of the IEEE International Symposium on Biomedical Imaging*, pp. 709–713, April 2017, Melbourne, Australia.

[7] A. E. Carpenter, T. R. Jones, M. R. Lamprecht, C. Clarke, I. H. Kang, O. Friman, D. A. Guertin, J. H. Chang, R. A. Lindquist, J. Moffat, P. Golland, and D. M. Sabatini, "CellProfiler: Image analysis software for identifying and quantifying cell phenotypes," *Genome Biology*, vol. 7, no. 10, pp. R100–1–11, October 2006.

[8] G. Litjens, T. Kooi, B. E. Bejnordi, A. A. A. Setio, F. Ciompi, M. Ghafoorian, J. A. van der Laak, B. van Ginneken, and C. I. Sanchez, "A survey on deep learning in medical image analysis," *Medical Image Analysis*, vol. 42, no. 1, pp. 60–88, December 2017.

[9] O. Ronneberger, P. Fischer, and T. Brox, "U-Net: Convolutional networks for biomedical image segmentation," *Proceedings of the Medical Image Computing and Computer-Assisted Intervention*, pp. 231–241, October 2015, Munich, Germany.

[10] M. Z. Alom, C. Yakopcic, T. M. Taha, and V. K. Asari, "Microscopic nuclei classification, segmentation and detection with improved deep convolutional neural network (DCNN) approaches," *arXiv preprint arXiv:1811.03447*, pp. 1–18, November 2018.

[11] V. Badrinarayanan, A. Kendall, and R. Cipolla, "SegNet: A deep convolutional encoder-decoder architecture for image segmentation," *IEEE Transactions on Pattern Analysis and Machine Intelligence*, vol. 39, no. 12, pp. 2481–2495, January 2017.

[12] C. Fu, D. J. Ho, S. Han, P. Salama, K. W. Dunn, and E. J. Delp, "Nuclei segmentation of fluorescence microscopy images using convolutional neural networks," *Proceedings of the IEEE International Symposium on Biomedical Imaging*, pp. 704–708, April 2017, Melbourne, Australia.

[13] O. Cicek, A. Abdulkadir, S. S. Lienkamp, T. Brox, and O. Ronneberger, "3D U-Net: Learning dense volumetric segmentation from sparse annotation," *Proceedings of the Medical Image Computing and Computer-Assisted Intervention*, pp. 424–432, October 2016, Athens, Greece.

[14] F. Milletari, N. Navab, and S. A. Ahmadi, "V-Net: Fully convolutional neural networks for volumetric medical image segmentation," *Proceedings of the IEEE 2016 Fourth International Conference on 3D Vision*, pp. 565–571, October 2016, Stanford, CA.

[15] S. Lee, C. Fu, P. Salama, K. W. Dunn, and E. J. Delp, "Tubule segmentation of fluorescence microscopy images based on convolutional neural networks with inhomogeneity correction," *Proceedings of the IS&T International Symposium on Electronic Imaging*, vol. 2018, no. 15, pp. 199–1–199–8, January 2018, Burlingame, CA.

[16] J. Ribera, D. Guera, Y. Chen, and E. J. Delp, "Locating objects without bounding boxes," *Proceedings of the IEEE Conference on Computer Vision and Pattern Recognition*, pp. 6479–6489, June 2019, Long Beach, CA.

[17] D. Karimi and S. E. Salcudean, "Reducing the Hausdorff distance in medical image segmentation with convolutional neural networks," *arXiv preprint arXiv:1904.10030*, pp. 1–15, April 2019.

[18] J. Y. Zhu, T. Park, P. Isola, and A. A. Efros, "Unpaired image-to-image translation using cycle-consistent adversarial networks," *Proceedings of the IEEE International Conference on Computer Vision*, pp. 2242–2251, October 2017, Venice, Italy.

[19] Z. Zhang, L Yang, and Y Zheng, "Translating and segmenting multimodal medical volumes with cycle-and shapeconsistency generative adversarial network," *Proceedings of the IEEE Conference on Computer Vision and Pattern Recognition*, pp. 9242–9251, June 2018, Salt Lake City, UT.

[20] Y. Huo, Z. Xu, S. Bao, A. Assad, R. G. Abramson, and B. A. Landman, "Adversarial synthesis learning enables segmentation without target modality ground truth," *Proceedings of the IEEE International Symposium on Biomedical Imaging*, pp. 1217–1220, April 2018, Washington, DC.

[21] C. Fu, S. Lee, D. J. Ho, S. Han, P. Salama, K. W. Dunn, and E. J. Delp, "Three dimensional fluorescence microscopy image synthesis and segmentation," *Proceedings of the IEEE Conferences on Computer Vision and Pattern Recognition Workshop*, pp. 2302–2310, June 2018, Salt Lake City, UT.

[22] S. Han, S. Lee, C. Fu, P. Salama, K. W. Dunn, and E. J. Delp, "Nuclei counting in microscopy images with three dimensional generative adversarial networks," *Proceedings of the SPIE Conference on Medical Imaging*, pp. 109492Y–1–11, February 2019, San Diego, CA.

[23] S. Lee, S. Han, P. Salama, K. W. Dunn, and E. J. Delp, "Three dimensional blind image deconvolution for fluorescence microscopy using generative adversarial networks," *Proceedings of the IEEE International Symposium on Biomedical Imaging*, pp. 538–542, April 2019, Venice, Italy.

[24] A. Bansal, S. Ma, D. Ramanan, and Y. Sheikh, "Recycle-GAN: Unsupervised video retargeting," *Proceedings of the European Conference on Computer Vision*, pp. 122–138, September 2018, Munich, Germany.

[25] D. J. Ho, C. Fu, P. Salama, K. W. Dunn, and E. J. Delp, "Nuclei segmentation of fluorescence microscopy images using three dimensional convolutional neural networks," *Proceedings of the IEEE Conferences on Computer Vision and Pattern Recognition Workshop*, pp. 834–842, July 2017, Honolulu, HI.

[26] J. Canny, "A computational approach to edge detection," *IEEE Transactions on pattern analysis and machine intelligence*, , no. 6, pp. 679–698, 1986.

[27] D. P. Kingma and J. L. Ba, "Adam: A method for stochastic optimization," *arXiv preprint arXiv:1412.6980*, pp. 1–15, December 2014.

[28] P. A. Yushkevich, J. Piven, H. C. Hazlett, R. G. Smith, S. Ho, J. C. Gee, and G. Gerig, "User-guided 3D active contour segmentation of anatomical structures: Significantly improved efficiency and reliability," *NeuroImage*, vol. 31, no. 3, pp. 1116–1128, July 2006.